2023-06-26

Ultracold Neutral Plasma Evolution in an External Magnetic Field

Chanhyun Pak
Brigham Young University

Ultracold Neutral Plasma Evolution in an External Magnetic Field

Chanhyun Pak

A thesis submitted to the faculty of
Brigham Young University
in partial fulfillment of the requirements for the degree of

Master of Science

Scott Bergeson, Chair
Michael Ware
Ryan Camacho

Department of Physics and Astronomy

Brigham Young University

ABSTRACT

Ultracold Neutral Plasma Evolution in an External Magnetic Field

Chanhyun Pak
Department of Physics and Astronomy, BYU
Master of Science

We study the expansion velocity and ion temperature evolution of ultracold neutral plasmas (UNPs) of calcium atoms under the influence of a uniform magnetic field that ranges up to 200 G. In the experiments, we use a magneto-optical trap (MOT) to capture the neutral atoms and laser-induced fluorescence (LIF) to take images of the plasma. We vary the magnetic field strengths and the initial electron temperatures and observe the plasma evolution in time. We compare the ion temperature evolution to the theory introduced in the paper by Pohl et. al. [Phys. Rev. A 70, 033416 (2004)]. The evolution of the gradient of expansion velocity suggests the presence of ion acoustic waves (IAWs). We speculate that our measurements showing that the ion temperature remains relatively high throughout the evolution is a biproduct of the IAW.

Keywords: Coulomb coupling parameter, Debye screening length, ultracold neutral plasma, alkaline earth metals, magneto-optical trap, laser-induced fluorescence, Zeeman shift, frequency comb, Nd:YAG-pumped dye laser, Doppler shift, Doppler broadening, Voigt profile, ion acoustic waves.

ACKNOWLEDGMENTS

Dr. Bergeson: My endeavor in the field of AMO physics was mostly possible due to Dr. Bergeson. I could develop skills necessary for me to advance to the next stage in the research career by learning much from his enthusiasm and acute mind in approaching scientific problems, let alone learning from his deep knowledge in theory and much experience in the experiments. Thus, I am grateful to had had him as the master's program advisor.

Committee: I thank the committee members Dr. Bergeson, Dr. Ware, and Dr. Camacho for their precious time and effort to supervise and review my works and evaluate the master's thesis.

Brigham Young University: I am grateful to had spent three undergraduate years and two graduate student years to learn and experience what it is to become an engaged researcher and carpe diem. I feel priviledged to had studied here and to pay forward to the world with humble contributions to live up to the motto of the school, "Enter to learn, go forth to serve."

Funding agencies: I give many thanks to the support of our funding agencies that made this project financially possible; Air Force Office of Scientific Research under program AFOSR FA9550-17-1-0302, and the National Science Foundation under grant number NSF PHY-2009999.

Contents

List of Figures

List of Tables

Chapter 1

Introduction

Ultracold neutral plasmas are a useful platform for understanding strongly coupled Coulomb systems in a relatively slow time frame [1]. We use the Coulomb coupling parameter Γ to express the ratio between the electrical potential energy and the kinetic energy:

$$\Gamma = \frac{e^2}{4\pi\varepsilon_0 a_{WS}} \frac{1}{k_{\mathrm{B}} T}, \tag{1.1}$$

where e is the unit charge of the particles, ε_0 is the vacuum permittivity, a_{WS} is the Wigner-Seitz radius and can be expressed as the following:

$$a_{WS} = \left(\frac{3}{4\pi n}\right)^{1/3} \tag{1.2}$$

where n is the number density of the plasma. Another parameter $\kappa = a_{WS}/\lambda_D$ is the inverse scaled screening length [2], where $\lambda_D = \sqrt{\varepsilon_0 k_{\mathrm{B}} T/ne^2}$ is the Debye screening length. This is also used to describe plasma ion interaction. We can map many different kinds of plasmas in Γ-κ space and consider those plasmas in overlapping Γ-κ to be thermodynamically similar [3]. As an example, UNP overlaps in the Γ-κ space with some high energy density plasma (HEDP) for fusion that are generated in the National Ignition Facility (NIF) [3]. Thus, using UNPs can provide insights on understanding plasmas for fusion.

There are many studies done on the evolution of UNP; the creation [4], the theory [5–8], the electron screening [9], the electron temperature evolution in the UNP [10], the ion temperature [11], ion acoutic waves (IAWs) [12, 13], the crossover study between UNP and HEDP [3], the evolution of the UNP under magnetic field [14–16]. Reviews were written by Killian [1] and Lyon [2].

Studying the effects of the magnetic field on plasma has been a subject of interest in various sub-fields of plasma physics study [17–28], including the study of HEDP [29] and UNP [14, 30–33]. An initial study of the spatial distribution and the expansion velocity evolution of UNP under external magnetic field is presented by Sprenkle et. al. [16]. They attempted to use a self-similar plasma exansion model to explain the evolution of the partially magnetized UNP. It predicts the evolution in the parallel direction well. However, in the transverse evolution, there is a disagreement in predicting the plasma expansion velocity between the self-similar plasma expansion model and the phenomenological model that depends on the strength of the applied magnetic field. We extend the study of plasma evolution in external magnetic field by studying the ion temperature evolution and the hydrodynamic velocity.

In our experiment, we first create the UNP by trapping Ca atoms in a MOT, ionize them using pulsed lasers, and use lasers to probe the plasma using the method of LIF. LIF is a method of exciting atoms or ions and measuring the spontaneous emission. To create a uniform magnetic field, we use a pair of Helmholtz coils. We lock the laser frequencies to a frequency comb and control the timing of electronic devices using a pulse generator. The gradient of the hydrodynamic ion expansion velocity and the ion temperature is extracted from a line shape model fit to the LIF data. We observe the LIF when the probe laser propagates in directions parallel and transverse to the magnetic field direction. We use various strength of external magnetic field and vary the initial electron temperature, T_e, to map out the resulting evolution of the UNP.

We measure the fluorescence images, showing the ion Doppler shift for typically eleven different probe laser frequency detunings. For density measurements, these 11 images are summed together

and then projected onto either z-axis or x-axis the UNP for observing size evolution in the parallel direction or transverse direction respectively. For temperature and hydrodynamic velocity analysis, the fluorescence intensity in each pixeel, as a function of probe laser detuning, is fit to a Voigt profile. The center frequency and rms Gaussian widths are fit parameters. Using the Doppler shift, these are converted to hydrodynamic velocity and rms velocity (temperature).

In the Results section, we introduce a hydrodynamic theory from which we deduce a set of coupled differential equations for the evolution of the spatial distribution, expansion velocity, ion temperature, and electron temperature in asymmetrical Gaussian plasma distribution functions. The differential equations provide a prediction for the ion temperature evolution of the partially magnetized UNP which qualitatively agrees with experimental results.

In the partially magnetized UNP evolution, the gradient of the expansion velocity oscillates in time. We speculate that this is an IAW, or plasma mode. A relatively high ion temperature, compared to the unmagnetized case, is observed throughout the plasma evolution, consistent with IAW heating. The significance of our experiment is the careful measurement of the magnetized UNP evolution in both the parallel and the transverse directions, confirmation that the hydrodynamic theory qualitatively predicts the evolution of the ion temperature, and exploring the possibility of IAWs in magnetized UNP.

Chapter 2

Experimental Methods

2.1 Introduction

Alkaline earth metals, such as calcium and strontium, have been subjects of interest in AMO physics for their inherent properties due to their two-valence-electron structure. These properties provide narrowband transitions, which makes precise laser spectroscopy possible to study atomic clocks [34–37] and Bose-Einstein condensates [38, 39]. Calcium and strontium atoms can be used to build quantum-bits with high fidelity [40–42]. Trapping and ionization of the calcium atoms also take advantage of the structure of the two-valence electrons. There are several trapping method for calcium atoms, such as optically trapping [43] or using a MOT [44, 45].

In this section, we explain the experiment procedure and the details of the measurements. First, we trap the atoms by using the MOT which consists of anti-Helmholtz coils and six near-resonant continuous wave (CW) lasers. Then, two-photon ionization is used to ionize the Ca atoms to the ground state of Ca^+. We apply external magnetic field that is uniform in the z-direction to restrain the plasma expansion in the transverse direction. To observe the UNP evolution in either the parallel or the transverse direction, we use a weak probe laser beam at 393 nm that propagates either along

or transverse to the magnetic field directions. We vary the strength of the external magnetic field in the range of 0 G to 200 G. We vary the initial electron temperature from 50 K to 400 K. The study by Sprenkle et. al. [16] was limited to observing the evolution of the density distribution from which the expansion velocity of the plasma was calculated. The objective of our experiments is to broaden this study to observe the evolution of the ion temperature and the expansion velocity directly.

2.2 Trapping the Ca atoms

2.2.1 Magneto-optical trap

Before the formation of the plasma, it is necessary to capture atoms in place. While there are many different kinds of traps([46]) for neutral atoms such as magnetic traps, dipole force optical traps, and radiation pressure traps, we use magneto-optical trap. MOT is a hybrid of magnetic and optical trap, thus having feature from both kinds. The laser radiation produces a strong radiating force for laser cooling.

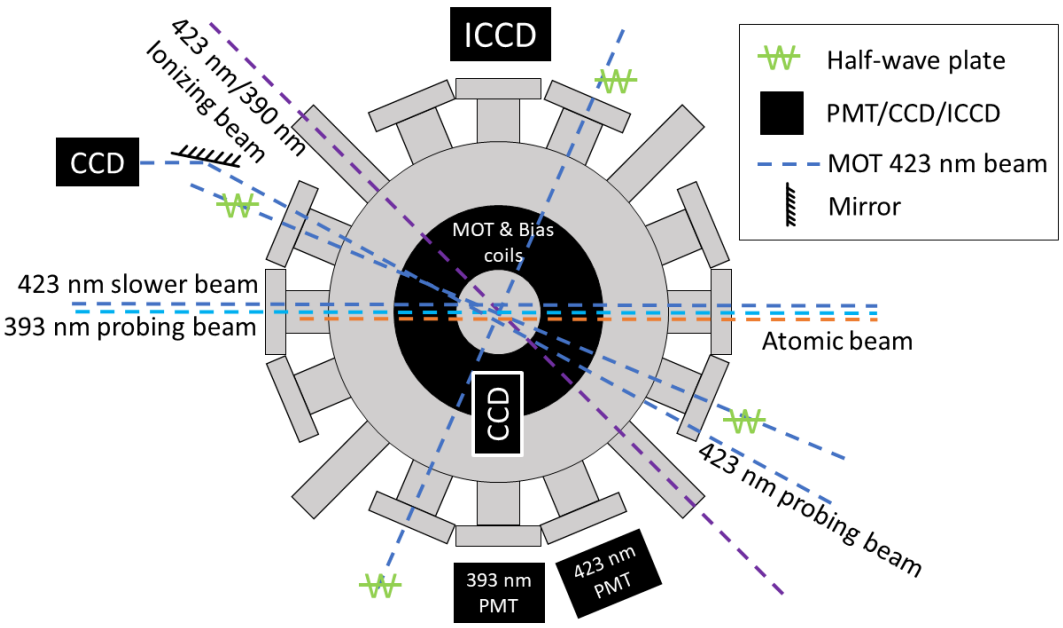

Figure 2.1 Bird's eye view on the vacuum chamber and the arrangement of optics.

We sublimate solid calcium atoms by heating a solid Ca source to 500 C°. The atomic beam is formed using an aligned microcapillary array, similar to what is described in the paper by Senaratne[47]. To reduce the velocity of the neutral atoms, a 423 nm "slower" laser beam is placed antiparallel to the atomic beam. The -304 MHz detuning of this laser beam from $4s^2\ {}^1S_0$ to $4s4p\ {}^1P_1$ Doppler-cools thermal atoms in the beam. The number of atoms in the MOT is increased because many atoms are Zeeman-shifted into resonance with the "slower" laser beam due to the fringing field of the MOT coil. The absorption of a photon by an atom entails the change of momentum, thus decreasing the velocity of the atom traveling parallel to the atomic beam. The excited calcium atoms have isotropic radiation probability, meaning that it has an equal probability of radiating a photon in a spontaneous emission process.

The magnetic part of MOT is an anti-Helmholtz pair of coils which creates a quadrupole magnetic field. The z-axis is the axis of symmetry of the quadrupole magnetic field and its equation

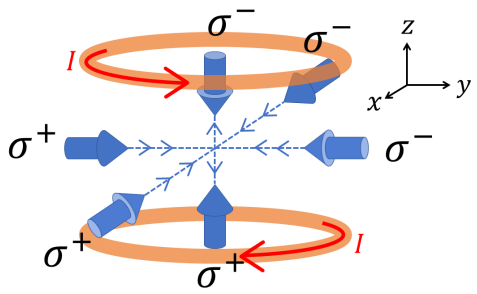

(a) Magneto-optical trap

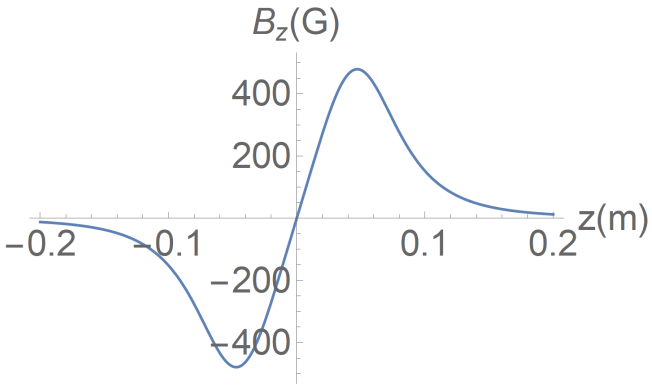

(b) Magnetic field in the z-direction.

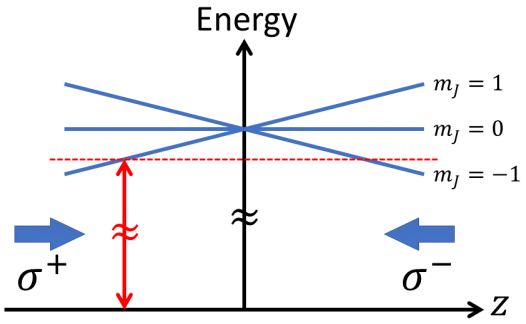

(c) Zeeman splitting and the laser cooling.

Figure 2.2 The MOT depicted in Fig. 2.2a consists of anti-Helmholtz coils with incoming 423 nm lasers in 6 orthogonal directions. Fig. 2.2b is a plot of quadrupole magnetic field in the z-direction of each experiment in the parallel and transverse direction. The gradient of the magnetic field in the center of the MOT was calculated to be 137.8 G/cm. Fig. 2.2c depicts the Zeeman splitting in the excited energy level $4s4p\ ^1P_1$ of an atom. The polarized beams $\sigma^{\pm}$ each corresponding to the sub energy level $m_j = \pm 1$ will resonate with the atom as a specific position in space and laser cool the atoms.

of the field in the z-direction is written as the following:

$$\mathbf{B}_z = \frac{1}{2}(I\mu_0 a^2)\left(\frac{1}{(a^2+(z-z_0)^2)^{3/2}} - \frac{1}{(a^2+(z+z_0)^2)^{3/2}}\right)\hat{\mathbf{z}}, \tag{2.1}$$

where a is the radius of a coil, z_0 is the distance of a coil away from the center of the MOT. From Eq. (2.1) we plot the strength of the magnetic field in Fig. 2.2b and can deduce that the magnetic field is linear near the center of the chamber. The following is the expansion in the Taylor's series:

$$\mathbf{B}_z \simeq \frac{3I\mu_0 a^2 z_0 z}{(a^2+z_0^2)^{5/2}}\hat{\mathbf{z}} = 137.8z\hat{\mathbf{z}}\ \text{G/cm}. \tag{2.2}$$

We see from Eq. (2.2), that magnetic field is approximately linear. The magnetic field of the MOT causes a Zeeman shift in the $4s4p\ ^1P_1$ energy level, splitting it into three states, $m_J = -1, 0, 1$. The presence of the magnetic field shifts the excited state energy by:

$$\Delta E = \langle V_{mag}(r)\rangle = \mu_B m_j B_{ext}, \tag{2.3}$$

which is also linear in space since B_{ext} is linear according to the approximation of Eq. (2.2).

The MOT uses a set of 423 nm laser beams from six sides that are detuned 54 MHz below the resonance with $4s4p\ ^1P_1$. The linear Zeeman shift results in a position-dependent force for the trap. The circularly polarized beams σ^+ and σ^- are respectively resonant with the $m = 1$ and $m = -1$ level at a particular location at space, as shown in Fig. 2.2c.

2.2.2 Extracting density and size information

We use the absorption imaging method to probe the neutral atoms in the MOT. To get the density and the size of the atom cloud, we use absorption imaging. In this method, we consider four different images. The 423 nm laser used for absorption f_{laser}, the photon absorption by the calcium atoms f_{abs}, the spontaneous emission by the calcium atoms $f_{s.e.}$, and the background signal and noise from all sources f_{dark}. Using these four images, we calculate the ratio between the intensity of the incident light and the transmitted light necessary for an absorption measurement. From Fig. 2.3a,

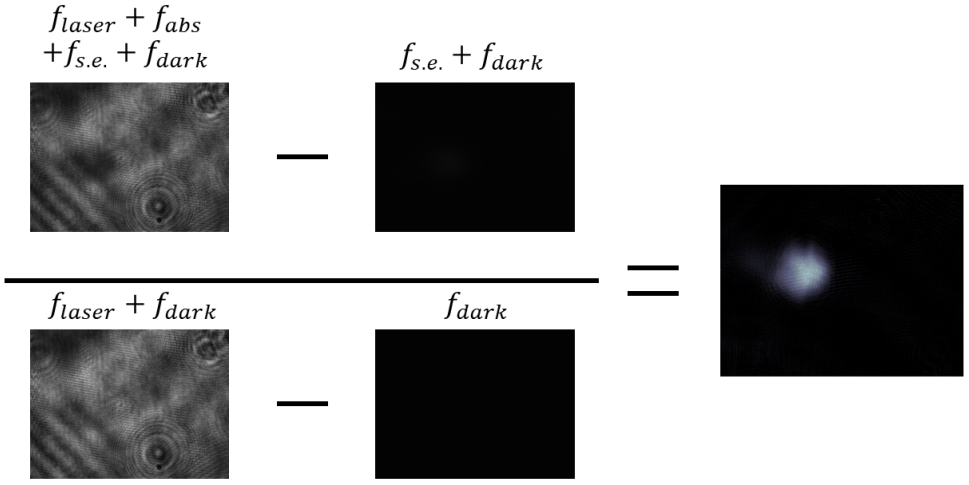

(a) Absorption images without the 424 nm laser repump

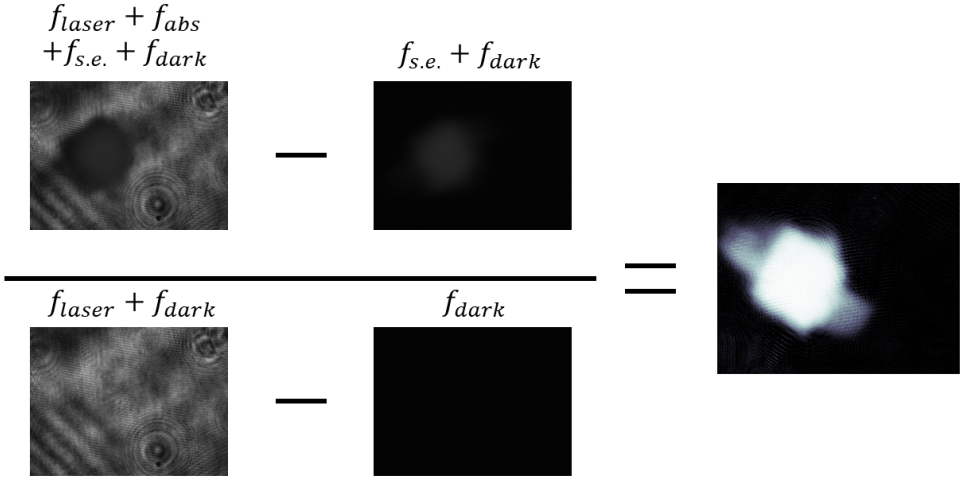

(b) Absorption images with 424 nm laser repump

Figure 2.3 The image $f_{laser} + f_{abs} + f_{s.e.} + f_{dark}$ is obtained when the 423 nm probing laser shutter and the MOT laser shutter are open. Image $f_{s.e.} + f_{dark}$ is when only the probing laser shutter is closed. Image $f_{laser} + f_{dark}$ is when only the MOT laser shutter is closed. Image f_{dark} is when both shutters are closed. We have an enhanced signal when we use the 424 nm repumper laser.

left top image is superposition of f_{laser}, f_{abs}, $f_{s.e.}$, and f_{dark}. Meanwhile, the right top image is taken after the 423 nm absorption laser is removed from the MOT. This image includes the fluorescence from the spontaneous emission from the excited calcium atoms and the background, $f_{s.e}$ and f_{dark}. Next, the left bottom is image is taken of the 423 nm absorption laser. It is a superposition of f_{laser} and f_{dark}. Lastly, the bottom right is f_{dark} when the MOT and absorption lasers are all blocked. The following equation calculates the absorption ratio:

$$\frac{(f_{laser}+f_{abs}+f_{s.e.}+f_{dark})-(f_{s.e.}+f_{dark})}{(f_{laser}+f_{dark})-f_{dark}} = \frac{f_{laser}+f_{abs}}{f_{laser}} = \frac{I_f(x,y)}{I_0} \tag{2.4}$$

This ratio of the incidence intensity over the transmitted intensity is used to calculate the optical depth (OD) that is related to Beer's law:

$$\text{Beer's law: } I_f = I(\infty) = I_0 e^{\int_{-\infty}^{\infty} n\sigma dz} \tag{2.5}$$

$$OD(x,y) \equiv \ln\left(\frac{I_0}{I_f}\right) = \int_{-\infty}^{\infty} \sigma n_0(x,y)\exp(-z^2/2r_0^2)dz \tag{2.6}$$

where σ is the absorption cross section, I_0 is the incident intensity, I_f is the transmitted intensity calculated previously. Also, here we assumed that the density has a Gaussian profile with the rms width of r_0 and the peak density n_0. Solving this equation for the peak density over the entire space we have:

$$n_0 = \frac{1}{\sigma r_0\sqrt{2\pi}}\ln\left(\frac{I_0}{I_f}\right) \tag{2.7}$$

In Eq. (2.7), the r_0 is the rms size of the Gaussian. This equation is used to find the size and the density of the neutral atom cloud. In our experiments, the typical density is 1.5×10^{10} cm^{-3} and the rms radius is typically 300 μm without the 424 nm repumper.

2.2.3 Branching ratio and re-pumping

The density in the order of 10^{10} cm^{-3} and the rms radius 300 μm are sufficient scales to carry out the experiments. However, we can enhance the fluorescence of the images and increase the signal to noise ratio by increasing density and the rms radius of the atom cloud using a re-pumping laser. By understanding the branching ratio of the spontaneous emission transitions we can implement necessary re-pumping lasers with appropriate wavelengths. The Table 2.1 is from the Yu et. al. [48]:

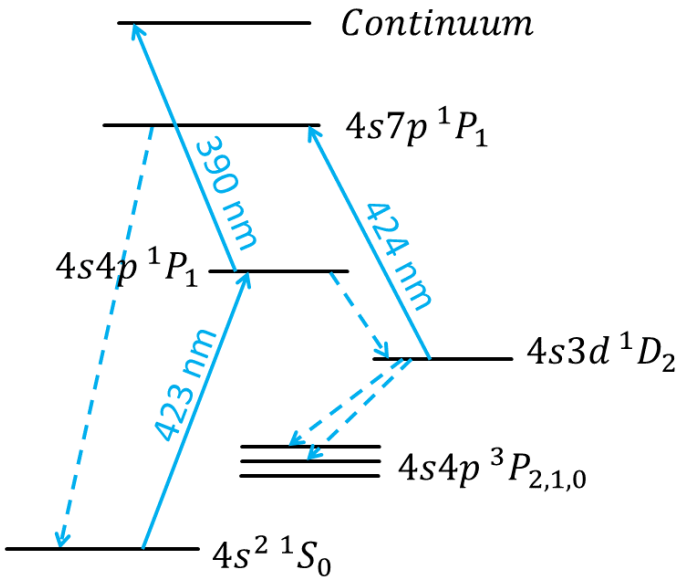

Figure 2.4 The schematic of the state transition including the repumping.

After the atoms are excited from the $4s^2\ ^1S_0$ to $4s4p\ ^1P_1$, almost 100 % of atoms decay back to the ground state with the lifetime 4.6 ns, but some of the atoms by the probability of 0.002 % decay to $4s3d\ ^1D_2$ state, which has a lifetime of 1.8 ms. The lifetime is $4s3d\ ^1D_2$ state is shorter than the lifetime of the MOT, which is typically 10 ms. The $4s3d\ ^1D_2$ state decays to $4s4p\ ^3P_1$ which is has a lifetime of 0.37 ms and $4s4p\ ^3P_2$ which is metastable. Atoms in the $4s4p\ ^3P_2$ state are lost from the MOT. This reduces the number of atoms in the MOT. To prevent this, we use a 424 nm laser to excite atoms of the $4s3d\ ^1D_2$ state to $4s7p\ ^1P_1$ [49]. This state has lifetime of 33.5 ns back

Initial	Final	$L\,A_{if}(10^8)\mathrm{s}^{-1}$	BR. (%)	lifetime
$4s4p\ ^3P_1$	$4s^2\ ^1S_0$	2.7380E-05	100	0.37 ms
$4s4p\ ^1P_1$	$4s^2\ ^1S_0$	2.170E+00	100	4.6 ns
$4s4p\ ^1P_1$	$4s3d\ ^3D_1$	3.7670E-08	0.00	-
$4s4p\ ^1P_1$	$4s3d\ ^3D_2$	1.000E-07	0.00	-
$4s4p\ ^1P_1$	$4s3d\ ^1D_2$	5.341E-05	0.00	-
$4s7p\ ^1P_1$	$4s^2\ ^1S_0$	1.295E-01	55.13	$\sim$ 33.5 ns
$4s7p\ ^1P_1$	$4s5s\ ^1S_0$	1.135E-02	2.79	-
$\vdots$				
$4s7p\ ^1P_1$	$4s3d\ ^1D_2$	1.575E-01	38.64	-
$4s3d\ ^1D_2$	$4s4p\ ^3P_1$	4.059E-06	83.12	1.8 ms
$4s3d\ ^1D_2$	$4s4p\ ^3P_2$	8.245E-07	16.88	-

Table 2.1 Branching ratio is the probability of the transition between the states. To calculate the lifetime of a state, the inverse of the sum of the spontaneous emission rates (A_{if}) in length (L). The lifetime of $4s7p\ ^1P_1$ is an approximation considering only three major transitions out of many. This is part of the table from [48].

to the ground state $4s^2\ ^1S_0$ with the branching ratio approximately being 55.13 %. Typically, the enhanced density of the atoms in the MOT is 3.5×10^{10} cm^{-3} and the radius is typically 500 μm, corresponding to nearly 10^8 atoms in the MOT.

2.3 Two-photon ionization and spectroscopy

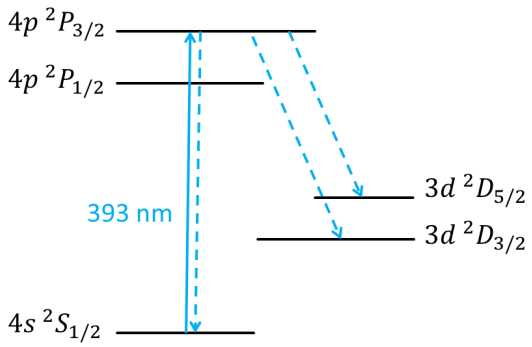

Figure 2.5 Partial energy level diagram for Ca^+.

Once the calcium atoms are trapped in the MOT, the MOT is turned off and the atom cloud expands for typically 1 ms before we ionize the calcium atoms using two-photon ionization process. The 423 nm and 390 nm pulses are generated using Nd:YAG-pumped dye lasers. The 423 nm laser beam excites the Ca atoms from the $4s^2\ ^1S_0$ to $4s4p\ ^1P_1$. Then, the 390 nm laser ionizes the calcium atoms in the excited state of 4s4p $^1P_1$ to the continuum. In our experiment, 99% of the neutral atoms are ionized.

We use the 393 nm laser for the laser-induced fluorescence measurement of the plasma ions. The 393 nm laser excites the Ca^+ ions from $4s\ ^2S_{1/2}$ to $4p\ ^2P_{3/2}$. In the mentioned atom density for the MOT before expansion which is in the order of 10^{10} cm^{-3}, the remaining neutral atoms do not result in any significant effect on the ions. The distribution of the ions is Gaussian and it expands self-similarly when there is no magnetic field. The typical density of the plasma is 10^9 cm^{-3} and the typical rms width of the plasma is 1 mm. The larger size and lower density come from the MOT expansion before ionization.

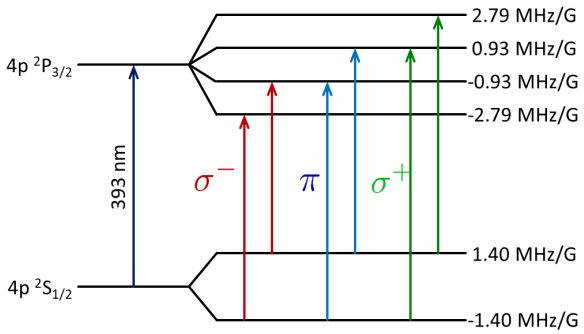

Figure 2.6 The external magnetic field results in Zeeman splitting. The perturbation is calculated in the units of frequency over the applied magnetic field (MHz/G). Polarizations of the 393 nm beam is given for respective resonant transitions.

In the presence of the magnetic field, Zeeman splitting must be considered in the LIF. In Fig. 2.6 is the energy diagram with the Zeeman splitting and we see that different transitions are resonant with different polarizations $\sigma^{\pm}$ and π. We used the $\sigma^{\pm}$ transitions for the experiment to observe the parallel plasma evolution. As in Fig. 2.6, the σ^- resonates with the $-1/2 \rightarrow -3/2$ and $1/2 \rightarrow -1/2$ transitions and the σ^+ resonates with the $-1/2 \rightarrow 1/2$ and $1/2 \rightarrow 3/2$ transitions. Thus, using the $\sigma^{\pm}$ polarization result in four peaks. We use either the $1/2 \rightarrow 3/2$ or the $-1/2 \rightarrow -3/2$ transitions in our analysis because they are optically closed. We fit these observed peaks to a Voigt profile to extract data.

We use π polarization to observe the plasma evolution in the transverse plane. In Fig. 2.6, we see that π polarization is resonated with the $1/2 \rightarrow 1/2$ and $-1/2 \rightarrow -1/2$ transitions. To enhance the signal in the experiment to observe the plasma evolution in the transverse direction, we used two 393 nm lasers to create four peaks with two of them coinciding in the frequency domain. We fit this superpositioned signal to a Voigt profile to extract data. In the experiment for the plasma evolution in the transverse plane, we also used the 424 nm repumping laser to increase the number of atoms in the $4s4p\ ^1P_1$ state, but we did not apply the repumper for the experiment for the plasma expansion in the parallel direction.

2.4 External magnetic field coils

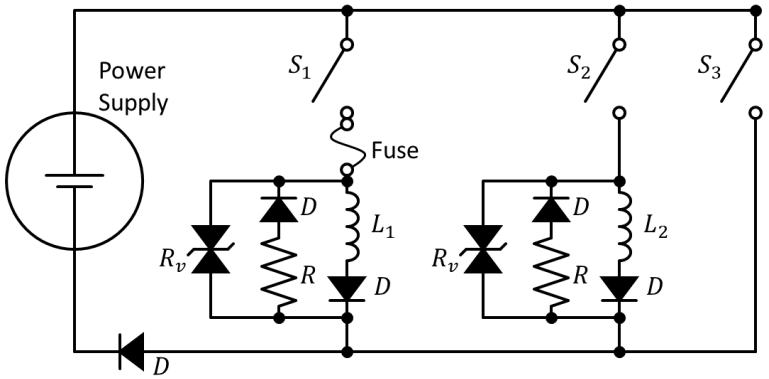

Figure 2.7 The schematic of the circuit for the bias magnetic field and the load inductors. L_1 and L_2 indicate the Bias coils and the loading coils respectively. The diodes D that is in series with resistors R are placed to mitigate the problem of high voltage spike when the switches are opened. The varistors R_v are also placed to cut the voltage spike.

For uniform external magnetic field, Helmholtz coils were place inside the vacuum chamber when we observed the parallel expansion, but they were removed from the vacuum chamber when observing the transverse expansion and put a bigger Helmholtz coils out side the chamber instead. The Helmholtz coils produce uniform magnetic field in the vertical direction. We also have load coils for the bias coils since we are concerned about the timing and it takes time to fully load the current for the maximum magnetic field the coils can create in the chamber. We also need to minimize the response of the power supply to the coils' back EMF. Thus, from Fig. 2.7, we first close S_3 and open S_1 and S_2. This runs the current through the short circuit. Approximately 5 ms before the ionizing laser pulse, we close S_2 and open S_3. This forces the current through the load coil, L_2. Finally, 0.5 ms before the ionizing laser pulse, we open S_2 and close S_1. This forces the current through the Helmholtz coils. This method of switching minimizes the impedance mismatch when the Helmholtz coils are active. For the parallel evolution experiment, we applied

the current up to 24 A in the coil which was situated in the vacuum chamber. For the transverse evolution experiment, we applied the current up to 250 A in the coil which situated outside the chamber. The linear relationship of the applied current to the generated magnetic field is 8.33 G/A for the experiment to observe the parallel expansion and we varied the current with the strength of 0, 6, 12, 18, and 24 A which correspond to 0, 50, 100, 150, and 200 G. We also varied the initial electron temperature to be 48 K and 96 K. For the transverse direction measurements, we have the current to be 0 A (to observe the symmetrical expansion in the tranverse direction) and 250 A (which corresponds to 183 G in the vacuum chamber) for the experiment to observe the transverse evolution but we varied the initial electron temperatures to be 0, 50, 100, 200, 400 K.

2.5 Calibration and Timing

2.5.1 Frequency Comb

Frequency comb is a useful tool for setting the frequency of the lasers. The absolute certainty of the frequency comb is 10 kHz [50, 51] in the near-infrared. To make use of the frequency comb, we offset lock one mode of the frequency comb to a Rb stabilized diode laser. Then, the other other lasers for the experiment such as 846, 780, and 786 nm lasers are offset locked to their nearest comb modes. Then the beat notes between the lasers and their nearest comb modes are measred to calculate the following equation:

$$f_{\text{laser}} = f_{\text{Rb}} \pm f_{\text{Rbb}} \pm N f_{\text{rep}} \pm f_{\text{beat}}. \tag{2.8}$$

where the f_{Rb} is the ^{87} Rb $D_2F = 2 \rightarrow F' = (2,3)$ crossover transition frequency of the Rb laser [52], f_{Rbb} is the beatnote between the Rb-stabilized diode laser and the nearest frequency comb mode, f_{beat} is the beat note between the near-infrared lasers in the fundamentals such as 846, 780, and 786 lasers and the nearest frequency comb mode, and N is an integer. The beatnote between the near-infrared lasers and the frequency comb is lock by an integral feedback lock circuit.

2.5.2 Timing on electronics

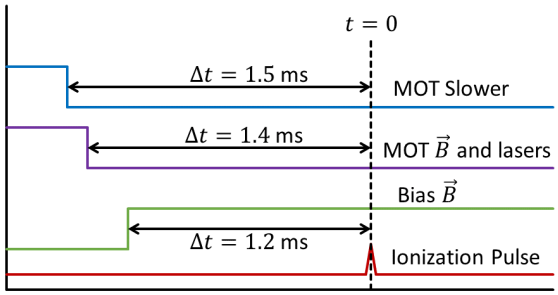

Figure 2.8 The schematic of the timing for the bias magnetic field.

We must set the right timing for the MOT to turn on and off, then wait for the time to load the current to the bias coils to create sufficient magnetic field strengths, and then ionize the atoms. Such timing is controlled by the pulse generator to send out voltage signal to AOM of the MOT and the slower, etc. Fig. 2.8 shows a schematic of the timing for the MOT slower, MOT magnetic field, bias magnetic field, and the laser pulse for ionization. We turn off the MOT slower and the MOT magnetic field 1.5 and 1.4 ms respectively before the ionization pulse. The bias magnetic field is turned on 1.2 ms before the ionization pulse.

2.6 The initial electron temperature

After the ionization, the initial kinetic energy of the electrons are converted into ion expansion energy in the evolution[10]. Thus, it is natural to investigate how different electron temperatures brings effect to the expansion of the UNP. To vary the initial temperature of the electrons, we use the 390 nm pulse laser. The excess energy of the photons above the ionization energy determines the initial kinetic energy of the electrons. Thus, we can control the initial electron temperature of the plasma by controlling the wavelength of the pulse lasers.

Chapter 3

Results

3.1 Introduction

In this chapter, we discuss applying the hydrodynamic theory introduced by Pohl et. al. [5] to our experiment. We modified the differential equations from the hydrodynamic theory to describe the asymmetrical evolution of the plasma. We compare the the theoretical result to the experimental outcome.

We also introduce an analysis method that merges the pixels from the images from an ICCD camera to bigger pixels to extract the information of the ion temperature and the plasma expansion velocity. The results of the analysis is then compared with hydrodynamic theory.

We confirm that the differential equations derived from the hydrodynamic theory qualitatively follows the behavior of the ion temperature evolution in the asymmetrical expansion. We also speculate the presence of the IAWs by comparing with the results reported from Killian et. al. [4].

3.2 The kinetic theory

The kinetic theory describing the behavior of the plasma is derived from the Vlasov model. The following references we use are specifically derived for UNPs: [5], [6], and [8]. The papers explain the UNP evolution with radial symmetry. However, the theories have a limit when there is a magnetic field. In our experiment, the magnetic field causes the asymmetry in the transverse direction. Some of the work done before our experiment is described in the paper by Sprenkle et. al. [16]. It includes studying the UNP evolution by observing the spatial density evolution in the parallel and the transverse direction. In the study, the expansions in both directions were identified to be self-similar. However, the behavior of the evolution did not follow the prediction of the theories such as the ambipolar diffusion model and the self similar magnetized plasma expansion model.

We start with the Vlasov model which describes the dynamic of the plasma using the $f_\alpha(\mathbf{r},\mathbf{v},t)$ as the distribution function of particles. We follow the derivation from the paper [5]. The Vlasov model can be written as:

$$\frac{\partial f_i}{\partial t} + \mathbf{v}\cdot\nabla_{\mathbf{x}} f_i + \mathbf{a}_i \cdot \nabla_{\mathbf{v}} f_i = 0. \tag{3.1}$$

In Eq. (3.1), the first term describes how the distribution changes over time, the second term considers the expansion velocity of the distribution, and the third term considers the acceleration of the distribution. According to the idea of Bogoliubov-Born-Green-Kirkwood-Yvon (BBGKY) hierarchy, a distribution of α-order particle can be describe with an integral of the degree of freedom other particles. In Eq. (3.1), this corresponds to the acceleration term. Pohl et. al. introduce this term as the integration of the Coulomb interaction of the charged particles in the distribution of $f_{\alpha\beta}$:

$$m_\alpha(\partial_t + \mathbf{v}\cdot\partial_{\mathbf{r}}) f_\alpha(\mathbf{r},\mathbf{v},t) = \sum_\beta \int [\partial_{\mathbf{r}}\varphi_{\alpha\beta}(\mathbf{r},\mathbf{r}')]\partial_{\mathbf{v}} f_{\alpha\beta}(\mathbf{r},\mathbf{v},\mathbf{r}',\mathbf{v}',t) d\mathbf{r}' d\mathbf{v}'. \tag{3.2}$$

The right-hand side of Eq. (3.2) includes $\varphi_{\alpha\beta} = q_\alpha q_\beta/|\mathbf{r}-\mathbf{r}'|$ which describes the Coulomb

interaction between the charge particles. Here, we apply near-equilibrium approximation:

$$f_e(\mathbf{r},\mathbf{v}) \propto \exp\left(\frac{\overline{\varphi}(\mathbf{r})}{k_{\mathrm{B}}T_e}\right)\exp\left(-\frac{\mathbf{v}^2}{2k_{\mathrm{B}}T_e}\right). \tag{3.3}$$

From Eq. (3.1)-(3.3), we derive a set of coupled differential equations that will be introduced in the following section.

3.2.1 Predicting the behavior of asymmetrical evolution

According to the paper by Pohl et. al. [5], when here is no magnetic field, we have the following equations from the hydrodynamic flow expansion model for the gradient of expansion velocity γ, the width of the plasma cloud σ, and the temperatures of ions and electrons respectively, T_i and T_e:

$$\frac{\partial\sigma^2(t)}{\partial t} = 2\gamma(t)\sigma^2(t), \tag{3.4}$$

$$\frac{\partial\gamma(t)}{\partial t} = \frac{k_B T_e(t) + U_{ii}(t)/3}{m_i\sigma^2(t)} - \gamma^2(t), \tag{3.5}$$

$$\frac{\partial T_i(t)}{\partial t} = -2\gamma(t)T_i(t) - \frac{2}{3}\left(\gamma(t)U_{ii} + \frac{\partial U_{ii}(t)}{\partial t}\right), \tag{3.6}$$

$$\frac{\partial T_e(t)}{\partial t} = -2\gamma(t)T_e(t), \tag{3.7}$$

where σ is defined in the ion distribution function f_e as

$$f_i(\mathbf{r},\mathbf{v}) \propto \exp\left(-\frac{r^2}{2\sigma^2}\right)\exp\left(-\frac{m_i(\mathbf{v}-\mathbf{u})^2}{2k_B T_i}\right), \tag{3.8}$$

the definition of the gradient of expansion velocity is given as

$$\mathbf{u} = \gamma\mathbf{r}, \tag{3.9}$$

and U_{ii} is the total correlation energy, m_i is the mass of an ion, and k_B is the Boltzmann constant. These are the differential equations for describing hydrodynamic expansion that is radially symmetrical. However, in our experiment, we apply uniform external magnetic field along the z-direction and the equations do not apply in our experiment with such condition. Thus, they must be modified to fit our situation. The magnetic field constrains the electrons, but not the ions. As a 0^{th}-order extension of this theory, we allow for an asymmetric expansion where it is radially symmetrical in the transverse plane, but considering a different rate of evolution in that plane compared to the evolution in the parallel direction. In this case, we modifiy Eq. (3.4)-(3.7) by applying:

$$f_i \propto \exp\left[-\left(\frac{x^2}{2\sigma_x^2}+\frac{y^2}{2\sigma_x^2}+\frac{z^2}{2\sigma_z^2}\right)\right]\exp\left[-\frac{m_i}{2k_B}\left(\frac{(v_x-\gamma_x)^2}{T_i}+\frac{(v_y-\gamma_x)^2}{T_i}+\frac{(v_z-\gamma_z)^2}{T_i}\right)\right], \quad (3.10)$$

and

$$\mathbf{u} = \gamma_x x\hat{\mathbf{x}} + \gamma_x y\hat{\mathbf{y}} + \gamma_z z\hat{\mathbf{z}}, \quad (3.11)$$

—notice how the condition is radially symmetric in the transverse plane, thus $\sigma_y = \sigma_x$ and $\gamma_y = \gamma_x$—resulting in a series of new equations:

$$\frac{\partial\sigma_x^2(t)}{\partial t} = 2\gamma_x(t)\sigma_x^2(t), \quad (3.12)$$

$$\frac{\partial\sigma_z^2(t)}{\partial t} = 2\gamma_z(t)\sigma_z^2(t), \quad (3.13)$$

$$\frac{\partial\gamma_x(t)}{\partial t} = \frac{k_B T_e(t) + U_{ii}(t)/3}{m_i\sigma_x^2(t)} - \gamma_x^2(t), \quad (3.14)$$

$$\frac{\partial\gamma_z(t)}{\partial t} = \frac{k_B T_e(t) + U_{ii}(t)/3}{m_i\sigma_z^2(t)} - \gamma_z^2(t), \quad (3.15)$$

$$\frac{\partial T_i(t)}{\partial t} = -\frac{4}{3}\gamma_x Ti - \frac{4}{9}\gamma_x U_{ii}/k_B - \frac{2}{3}\gamma_z Ti - \frac{2}{9}\gamma_z U_{ii}/k_B - \frac{2}{3}\frac{\partial U_{ii}}{\partial t}\frac{1}{k_B} + 2\frac{m_e}{m_i}\gamma_{ei}T_e, \quad (3.16)$$

$$\frac{\partial T_e(t)}{\partial t} = -\frac{4}{3}\gamma_x(t)T_e(t) - \frac{2}{3}\gamma_z(t)T_e(t) - 2\frac{m_e}{m_i}\gamma_{ei}(t)T_e(t), \tag{3.17}$$

where σ_x is the width of the plasma cloud in the x-direction and the y-direction considering radial symmetry in the transverse plane. Similarly, σ_z is the width of the plasma in the parallel direction to the magnetic field. The variables γ_x and γ_z are the gradient of expansion velocity respectively in the transverse plane and the parallel direction. The terms with the variable γ_{ei} are electron-ion thermalization terms introduced from McQuillen et. al. [8].

Theoretically, the electrons are constrained to move only along the magnetic field lines, we can require that there must be no change of the gradient of the expansion velocity in the transverse direction. This implies that the γ_x terms are set to zero in Eq. (3.12), (3.14), (3.16) and Eq. (3.17), resulting in an asymmetry of the evolution between the transverse plane and the parallel axis.

We solved the equations for the asymmetrical plasma evolution and plotted out the ion temperature over time in Python. The Python code is included in the appendix A. From Fig. 3.1, we see that this model predicts that the temperature in the asymmetric expansion of the UNP is higher than for the symmetric case after the initial DIH heating.

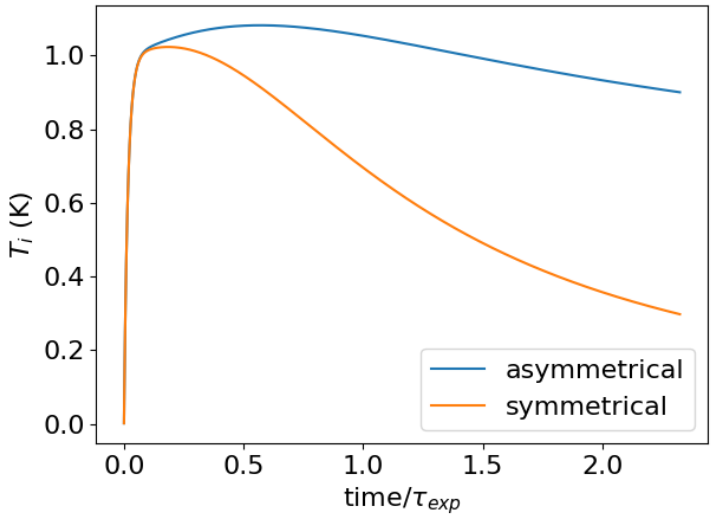

Figure 3.1 In the plot, the symmetrical evolution refers to the plasma expansion with radial symmetry in three orthogonal directions. The asymmetrical evolution refers to a case with an asymmetry in evolution rises from the constraint of the expansion in the transverse plane. The orange line for symmetric expansion is the application of the kinetic equations from Pohl et. al. [5] with the parameters suggested from McQuillen et. al. [8] where $n = 1.1 \times 10^{15}\text{m}^{-3}$, $T_e(0) = 50$ K, and $\tau_{\text{exp}} = 15\mu m$. The blue line representing the asymmetrical expansion has the same density and the initial eletron temperature and $\gamma_x = 0$ in Eq. (3.12), (3.14), (3.16), (3.17). Notice the time is in a scaled unit.

3.3 Analysis

After the ionization of the neutral atoms, the plasma expands with the kinetic energy resulted from the disorder-induced heating (DIH). In Fig. 3.2a, at early times, such as 0.5 μs, the plasma is relatively small and the expansion velocity is relatively slow. This implies that most of the ions do not have a significant magnitude of velocity in the parallel direction to the 393 nm probing laser. Thus, most part of the plasma is resonant to the probing laser and thus we have a round shape captured in ICCD, just like the image of 0.5 μs and 0 MHz detuning from Fig. 3.2b. At later times, such as 20 μs, the expansion velocity is higher. This implies that the ions with the velocity in the z-direction that is resonant to the probing laser is a thin line. From Fig. 3.2a and Fig. 3.2b, we see

that as the frequency of the 393 nm laser is detuned, the regions of the plasma that is resonant to the probing laser is different. For example, at +40 MHz detuning, the ions in the lower part of the plasma is traveling away from the probing laser, Doppler shifted in resonance. The fluorescence of the plasma is captured with ICCD camera with its pixel size being 13 μm. The thickness of the line indicate the distribution of the different kinetic motion of each particle, which is related to the temperature of the plasma. We measure the Doppler shift of the plasma to calculate the temperature of the ions. Also, the amount of distance the line is moving in the ICCD images along the frequency detuning tells us the information of how fast the plasma is expanding.

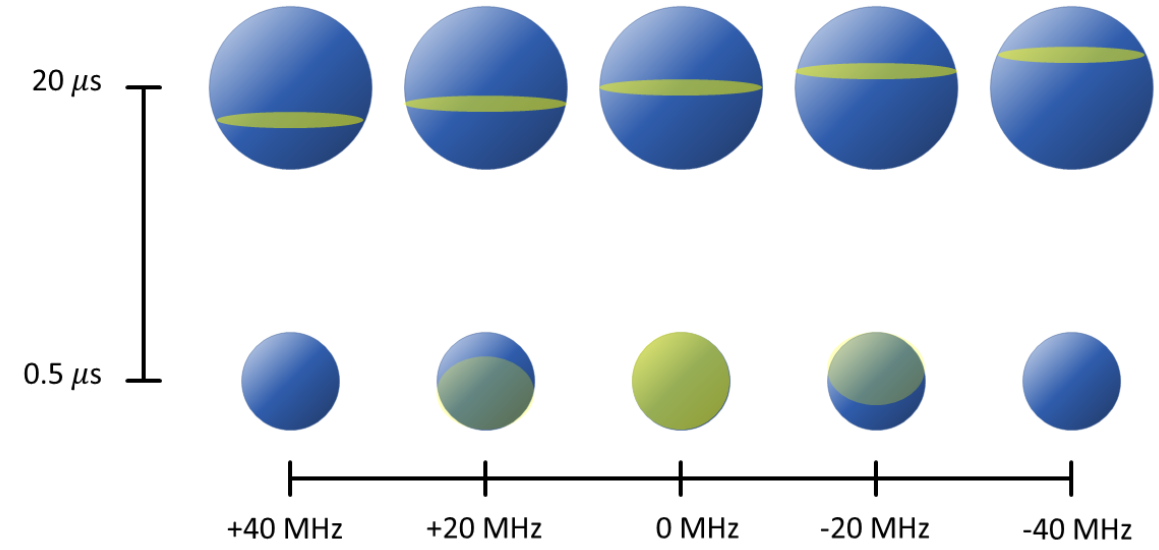

(a) Plasma expansion in time and its resonance with the detuning in the fundamental.

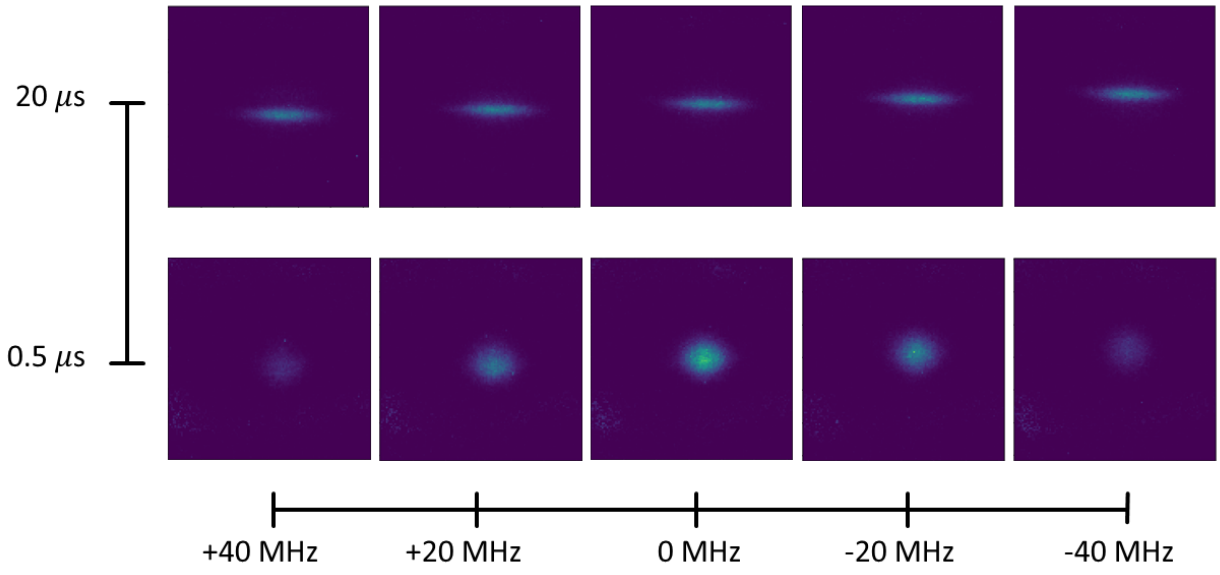

(b) ICCD images of UNP expansion and their resonances with the detunings.

Figure 3.2 The schematic of the UNP expansion and the detuning of frequency resonated into fluorescence captured from the ICCD. For these images, the probing laser is directed downwards. The expansion velocity is mapped in coordinate space due to the fact that the gradient of expansion velocity γ is proportional to the positioin in space r. In other words, expansion velocity $u(t) = \gamma(t)\mathbf{r}$, where $\gamma(t) = (t/\tau^2)/(1+t^2/\tau^2)$. Both ion temperature and the hydrodynamic expansion velocity contribute to the resonance in the images. In the early stage of the evolution, the ion temperature is dominant, while, in the late stage of the evolution, the expansion velocity is dominant.

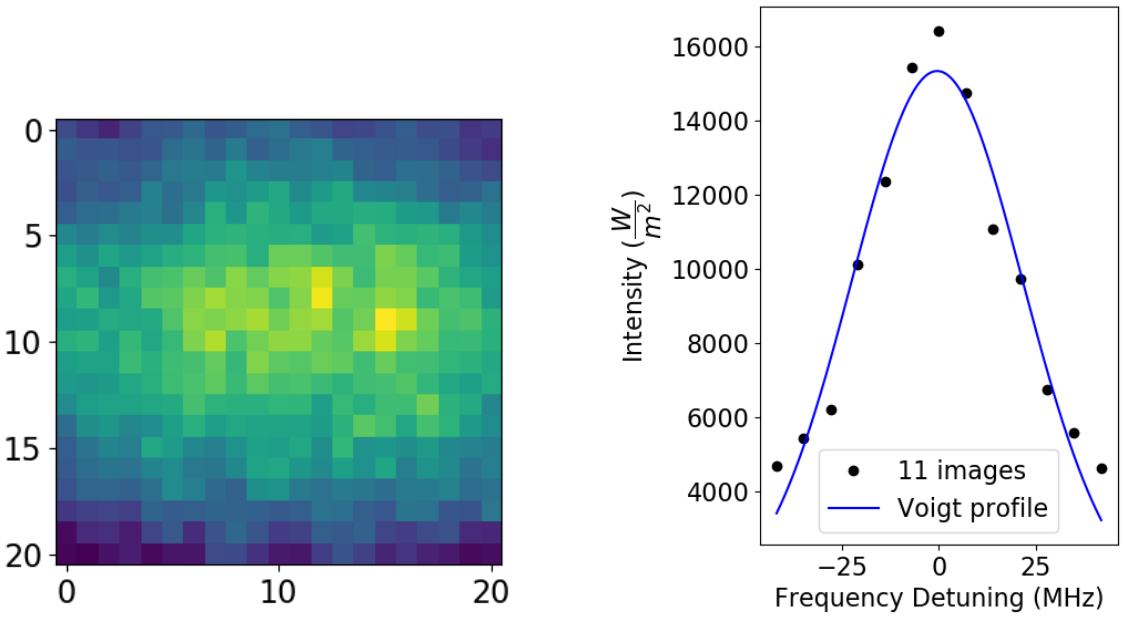

(a) An image that is the sum of all the images for different detuning frequencies.

(b) The intensities of the center pixel over the different frequency detunings are fit to a Voigt profile.

Figure 3.3 Pixel analysis.

To capture these desired sets of information, we do not use raw ICCD image, rather we merge small pixels to bigger pixels to create and use these 'super pixels' for convenience. Fig. 3.3a is the fluoresence image that is summed over all the detuning frequencies with the fluoresence signals given in super pixels. We combine several neighboring pixels to create into a super pixel with its value being the average of the values of the combined pixels. Using these super pixels we measure how the fluorescence intensity changes in each pixel along the frequency detuning. The change of intensity is shown in Fig. 3.3b. We fit this intensity vs. laser frequency to a Voigt profile. We extract the rms Gaussian frequency width and use it to calculate the ion temperatures. To calculate the expansion velocity of the plasma, we use the fitted center frequency of the Voigt profile. We convert the units from frequency to velocity using the Doppler shift.

Voigt profile is the convolution of the Gaussian function and the Lorentzian function. In the

experiment, we consider the velocity distribution of the atom cloud which can be read in the frequency distribution:

$$V(\nu) = \int L(\nu - \nu')G(\nu')d\nu', \tag{3.18}$$

where ν is the frequency and the L and G are each Lorentzian and Gaussian function:

$$L(\nu) = \frac{\delta/\pi}{\nu^2 + \delta^2} \tag{3.19}$$

and

$$G(\nu) = \frac{1}{\sqrt{2\pi}\nu_{rms}} e^{\nu^2/2\nu_{rms}^2}. \tag{3.20}$$

where δ is power-broadened natural half linewidth

$$\delta = \delta_N \sqrt{1 + I/I_{sat}}. \tag{3.21}$$

In our experiment, the value of $\delta_N = 11.49/2$ MHz in the laser fundamental and $I_{sat} = 50$ mW/cm^2 [53].

We extract the frequency information from the Gaussian distribution above to calculate the ion temperature in the following equation:

$$T_i = \frac{m_i(\nu_{rms}\lambda)^2}{k_\mathrm{B}}. \tag{3.22}$$

In the equation ν_{rms} is the rms Gaussian width, measured in the fundamental (786 nm), and λ is the wavelength of the laser in the fundamental (786 nm). This equation was derived from equating the kinetic energy with the thermal energy:

$$k_\mathrm{B}T_i = m_i v^2 = m_i(\nu_{rms}\lambda)^2. \tag{3.23}$$

3.4 Evolution along the parallel axis

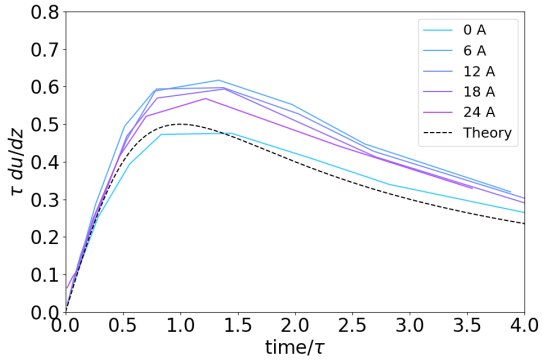

(a) The scaled gradient of the expansion velocity, 48 K.

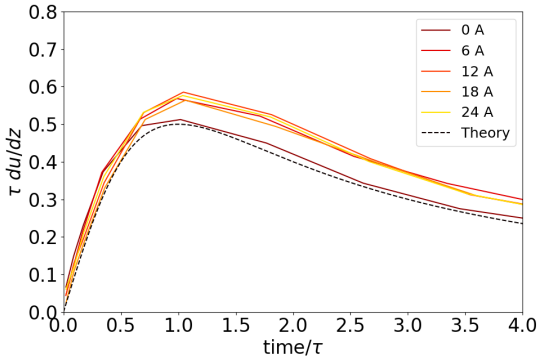

(b) The scaled gradient of the expansion velocity, 96 K.

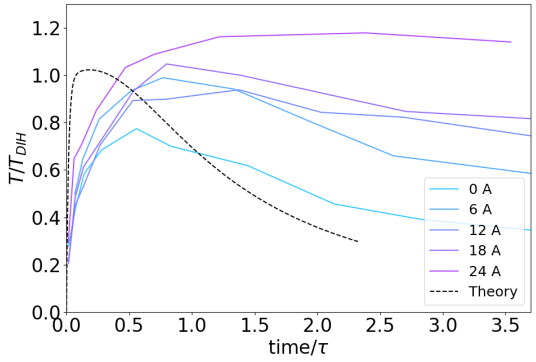

(c) The scaled ion temperature, 48 K.

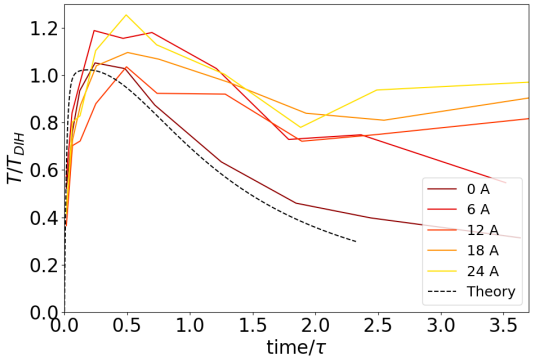

(d) The scaled ion temperature, 96 K.

Figure 3.4 The applied current through the coils are 0, 6, 12, 18, and 24 A and they correspond to 0, 50, 100, 150, and 200 G respectively. The plots of the scaled gradient of expansion velocity and the scaled ion temperatures for $T_e(0) = 48$ K and 96 K. The black dotted lines in Fig. 3.4a,Fig. 3.4b, Fig. 3.4c and Fig. 3.4d are according to the hydrodynamic flow expansion theory from Pohl et. al. [5].

We first introduce the experiment which we observe the evolution of the plasma in the parallel direction, using the $\sigma^{\pm}$ polarization and its resonating energy transitions. In this experiment, we had external magnetic field with the strength of $0, 50, 100, 150, 200$ G as a varying parameter and we also tried for two temperatures, 48 and 96 K. Fig. 3.4 are the scaled gradient of the expansion

velocity and scaled ion temperature evolving in time. In Fig. 3.4 we observe that the gradient of the expansion velocity follows the universal curve that is a description of the hydrodynamic expansion from Pohl et. al. [5] when the external magnetic field isn't applied. However, gradient of the velocity is slightly higher when the external magnetic field is applied. Fig. 3.4c and 3.4d are the plots of the temperatures scaled to the disorder-induced heating temperature, T_{DIH}. In Fig. 3.4c and Fig. 3.4d, the T_{DIH} are calculated as the following:

$$T_{DIH} = \frac{e^2}{4\pi\varepsilon_0 a_{WS}\Gamma k_B} \tag{3.24}$$

where Γ is the Coulomb coupling parameter assigned to be $\Gamma = 2.3$. The Wigner-Seitz radius $a_{WS} = (3/(4\pi n_{plasma}))^{1/3}$ where the number density of the plasma n_{plasma} is calculated by the following :

$$n_{plasma} = n_{atom}(\frac{\sigma_{atom}}{\sigma_{plasma}})^3 \tag{3.25}$$

where n_{atom} is the number density of the atom cloud and σ_{plasma} and σ_{atom} are the rms width of the plasma and the atoms cloud respectively. The calculation of the characteristic time τ_{exp} is as the following [1]:

$$\tau_{exp} = \sqrt{m_i\sigma(0)^2/k_B[T_e(0)+T_i(0)]}. \tag{3.26}$$

When the magnetic field is not applied, the ion temperature evolution follows closely, but not exactly the universal curve model since the model does not consider collisions [1, 8]. When the external magnetic field is applied, the ion temperature does not decrease quickly at late times and maintains relatively high temperature.

The phenomena that the ion temperature is staying high is consistent with the prediction from the Python code and the resulting plot, Fig. 3.1. However, the limit of the equations that predicts this phenomena does not take a magnetic field as a independent variable. A necessary model to connect the strength of the magnetic field to the asymmetric evolution of the plasma must be developed in a future study.

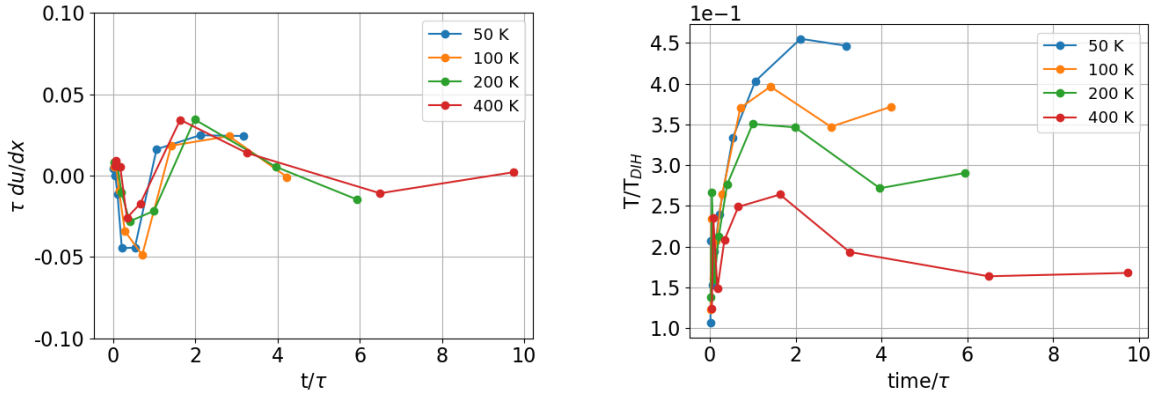

(a) The scaled gradient of the expansion velocity in the transverse direction averaged over the central 1.2 mm of the plasma.

(b) The scaled ion temperature evolution in the transverse direction.

Figure 3.5 The plots of the UNP evolution in the transverse direction.

3.5 Evolution along the transverse plane

In the experiment to observe the plasma expansion in the transverse direction to the external magnetic field, we applied the magnetic field with the strength of 183 G which is equivalent to the current with the strength of 250 A in the coils. We varied the initial electron temperature to be 0, 50, 100, 200, and 400 K.

In Fig. 3.5, when the external magnetic field is not applied, the scaled gradient of the expansion velocity $\tau \frac{du_x}{dx}$ follows the model. However, when the external magnetic field is applied, it seems that the scaled data all follow one universal curve that oscillates and decays with time. We also present the temperature evolution in the transverse plane. When the magnetic field is not applied, the ion temperature surges due to the disorder-induced heating in the earlier times and drops rapidly after $t/\tau > 1$. However, when the external magnetic field is applied, the ion temperature evolution behaves differently and maintains relatively high temperature.

In the following section, we attempt to explain the qualitative behavior of the gradient of the expansion velocity as the ion acoustic wave and use the ion temperature evolution as a supporting evidence of the presence of the ion acoustic wave.

3.5.1 Ion acoustic wave theory

Studying the ion acoustic waves are useful for studying the dispersion relationship of the strongly coupled systems [12, 13].The IAW frequency has the following dispersion relation:

$$\left(\frac{\omega}{k}\right)^2 = \frac{k_B T_e/m_i}{1+k^2\lambda_D^2} \tag{3.27}$$

where m_i is the ion mass and λ_D is the Debye screening length $\lambda_D \equiv \sqrt{\varepsilon_0 k_B T_e/n_e e^2}$ with the electron density n_e and charge e. In the long-wavelength limit, this takes the form of an ion acoustic waves with $\omega = k\sqrt{k_B T_e/m_i}$.

3.5.2 Evolution of the gradient of the expansion velocity

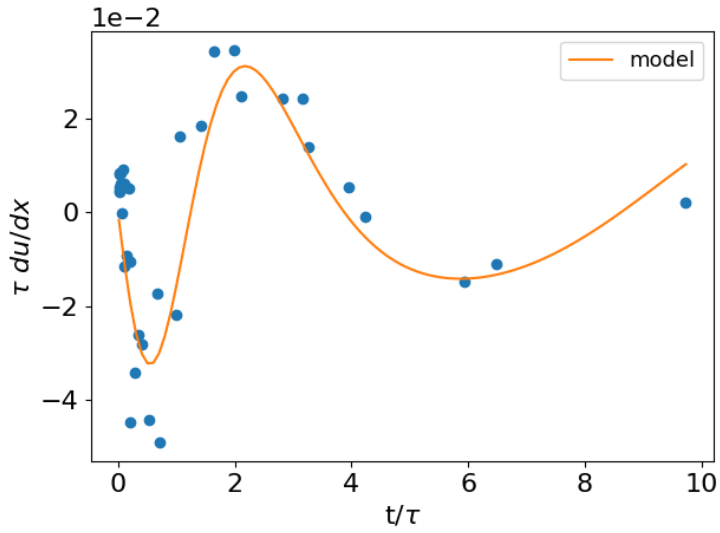

Figure 3.6 The blue dot indicates the points of all the scaled gradient expansion velocity for different initial electron temperatures. The orange line is purely phenomenological fitting. The model function $A(t) = A_0 e^{-\Gamma' \eta} \sin(a e^{-b\eta} \eta)$, where $\eta = t/\tau$. The fitting parameters are $A_0 = -4.377e-2$, $\Gamma' = 0.1965$, $a = 4.2848$, $b = 0.3845$.

In Fig. 3.5a, we observe the gradient of the expansion velocity to oscillate in time instead of a rapid surge and then the decay, thus implying the restraint in the transverse UNP expansion. This oscillation slightly resembles the ion acoustic wave oscillation that was created by a spatial modulation in the paper of Killian et. al. [13]. We speculate that a plasma mode is initiated in the magnetized plasma. In the paper of Killian et. al. [13] the following phenomenological equations are suggested for fitting the evolution expansion velocity of the ion acoustic wave:

$$u_{IAW} = \frac{\omega}{k} A_0 e^{-\Gamma t} \sin(kx) \sin(\omega t) \tag{3.28}$$

where ω and k are time dependent:

$$k(t) = \frac{k_0}{(1 + t^2/\tau_{\text{exp}}^2)^{1/2}} \tag{3.29}$$

and

$$\omega = k(t)\sqrt{k_B T_e(t)/mi}, \tag{3.30}$$

where Eq. (3.30) is a long wavelength limit ($\lambda_D \ll \lambda$), k_0 is a fit parameter, and $\tau_{\exp} = \sqrt{m_i\sigma/k_B(T_e+T_i)}$. We modify Eq. (3.28) to fit the plot in Fig. 3.6. We take the derivative of Eq. (3.28), then let the $x = 0$ and use the scaled unit time $\eta = t/\tau$:

$$\tau\frac{du_{IAW}}{dx} = \frac{A_0}{(1+\eta^2)^p}e^{-\Gamma'\eta}\sin\left(\frac{\eta}{(1+\eta^2)^q}\right), \tag{3.31}$$

where A_0 and Γ are fit parameters and $p, q = 1/2$ or 1 depending on deciding whether the k and Te is time-dependent. However, the data does not fit well to the model.

We also tried developing a purely phenomenological model following the traits of the gradient of the expansion velocity. We focuse on three traits of the evolution:

1. Oscillation in time $\rightarrow \sin(\omega t)$
2. The frequency $\omega(t)$ decays with time $\rightarrow \omega(t) = e^{-\alpha t}$, where $\alpha > 0$.
3. The Amplitude decays with time $\rightarrow A(t) = A_0 e^{-}\Gamma t$.

Thus, we can build the following model:

$$\tau\frac{du_{IAW}}{dx} = A_0 e^{-\Gamma'\eta}\sin(ae^{-b\eta}\eta), \tag{3.32}$$

where A_0, Γ', a, and b are fit parameters. We could find the value of the parameters, however, the it is left for the future to study if this model and the pertaining parameter values are physically meaningful.

3.5.3 Excessive heat in the ion temperature evolution

In addition to the evolution of the gradient of the expansion velocity, the ion temperature evolution that maintains relatively high temperature over time suggests that we have IAW in our experiments. In our experiment the ion temperature is isothermal and in Fig. 3.4c and Fig. 3.4d, we observed that the ion temperature is high throughout the plasma evolution in the parallel direction. Also, in Fig. 3.5b we observe the high temperature in the transverse evolution. The work by Killian et. al. [4] demonstrates that spatial density modulations create ion acoustic heating. Similarly, we speculate that the IAW observed in Fig. 3.5a causes heating. In Fig. 3.5b, we see that the initial electron temperature influences the ion temperature. This is also left as a challenge for a future study.

Chapter 4

Conclusion

We successfully created a Ca UNP in a MOT and we took images of the UNP evolution in a magnetic field using the LIF method. We had two types of experiments, one for observing the UNP evolution in the parallel direction and other for observing the transverse direction. In the experiment for observing the parallel direction, the magnetic field strengths 0, 50, 100, 150, and 200 G were applied and we also had the experiments for 48 and 96 K initial electron temperatures. In the experiment for observing the transverse direction, the magnetic field strengths were 0 G or it was fixed to be 183 G. We varied the electrons temperatures to be 0, 50, 100, 200, and 400 K. The images of the evolution were analyzed using a Voigt profile from which we extracted the Doppler broadening, that can be converted to the temperature of the plasma, and the hydrodynamic expansion velocity. We compared the experimental result to the theory of the hydrodynamic flow expansion model by Pohl et. al. [5]. We also used the study of Killian et. al. [13] to explore the possibility of IAWs in our UNP.

We modified a set of differential equations for symmetric expansion that are derived from the hydrodynamic flow expansion theory so that it describes the case for asymmetric expansion.

The modified differential equations predict the evolution of the ion temperature when the magnetic field is applied in the parallel direction. The limitation of the model is that we did not use the magnetic field as an independent variable when describing the asymmetry.

Our measurement of the gradient of expansion velocity in the transverse direction when the magnetic field is applied seemed to point to the presence of IAWs. When the gradient of expansion velocity is scaled using the characteristic expansion time τ, data forms one evolution line, suggesting the evolution of an IAW. We attempted to fit our experimental results to the IAW model suggested by Killian et. al. [13], but we were unsuccessful. In the same paper by Killian, it also explains that the additional heating comes from the IAW motion due to the density modulation in space. We speculate that the heating that we observe in the UNP evolution in our experiments indicates the presence of the IAWs.

In conclusion, our research using UNP has been successful in confirming the theory of hydrodynamic flow expansion in an asymmetrical evolution, but we were not successful in clearly identifying whether the UNP evolution in the magnetic field has IAW in it. The challenge of the future work is to connect the asymmetry of the differetial equation with the magnetic field.

Appendix A

Python code

```
# -*- coding: utf-8 -*-
"""
Created on Fri Apr 28 23:01:29 2023

@author: Chanhyun Pak
"""


from scipy.integrate import odeint
import numpy as np
import matplotlib.pyplot as plt

plt.close('all')
plt.rcParams.update({'font.size': 16})

# constants
kb      = 1.38e-23
mi      = 88*1.661e-27 # in kg
me      = 9.11e-31 # in kg
```

```
20 e       = 1.6e-19
21 eps0    = 8.85e-12
22 n0      = 1.1e15 * 0.5 # Killian paper Fig. 5 (a) # Changing this to 0.1e15
       brought it closer.
23 sigma0x = 0.001035
24 sigma0z = 0.001035
25 Ti0     = 0.002
26 #tauexp = 15e-6   # Killian paper Fig. 5 (a)
27 tauexp = np.sqrt(mi*sigma0x**2/kb/(50)) # ours
28
29 def odes(x, t):
30
31   # assign each ODE to a vector element
32   sigmax = x[0]
33   sigmaz = x[1]
34   gammax = x[2]
35   gammaz = x[3]
36   Uii    = x[4]
37   Ti     = x[5]
38   Te     = x[6]
39
40
41   # define other variables
42   n = n0 * (sigma0x**2 / sigmax**2)**(2/2)*(sigma0z**2 / sigmaz**2)**(1/2)
43   aws    = (4*np.pi*n/3)**(-1/3)
44   omega  = np.sqrt(n*e**2/me/eps0)
45   tau    = np.sqrt(mi*eps0/e**2/n)
46   Gammae = e**2/(4*np.pi*eps0*aws)/(kb*Te)
47   Lambda = 1/np.sqrt(3)/Gammae**(3/2)
48   gammaei = np.sqrt(np.pi) * np.sqrt(2/(3*np.pi))*Gammae**(3/2)*omega*np.
```

```
 log(Lambda)
Gamma  = e**2/(4*np.pi*eps0*aws)/(kb*Ti)
A1     = -0.9052
A2     = 0.6322
A3     = -np.sqrt(3)/2-A1/np.sqrt(A2)
Uiieq  = kb*Ti*Gamma**(3/2)*(A1/np.sqrt(A2+Gamma)+A3/(1+Gamma))


# define each ODE
# dsigmaxdt = gammax*sigmax
dsigmaxdt = 0
dsigmazdt = gammaz*sigmaz

# dgammaxdt = (kb*Te+Uii/3)/(mi*sigmax**2)-gammax**2
dgammaxdt = 0
dgammazdt = (kb*Te+Uii/3)/(mi*sigmaz**2)-gammaz**2

dUiidt = -(Uii-Uiieq)/tau

# dTidt = -2*gamma*Ti-2/3/kb*(gamma*Uii+dUiidt)+2*me/mi*gammaei*Te
# dTidt = -4/3*gammax*Ti-4/9*gammax*Uii/kb-2/3*gammaz*Ti-2/9*gammaz*Uii/
 kb-2/3*dUiidt/kb+2*me/mi*gammaei*Te
dTidt = -2/3*gammaz*Ti-2/9*gammaz*Uii/kb-2/3*dUiidt/kb+2*me/mi*gammaei*
 Te

# dTedt = -2*gamma*Te-2*me/mi*gammaei*Te
# dTedt = -4/3*gammax*Te-2/3*gammaz*Te-2*me/mi*gammaei*Te
dTedt = -2/3*gammaz*Te-2*me/mi*gammaei*Te

return [dsigmaxdt, dsigmazdt, dgammaxdt, dgammazdt, dUiidt, dTidt, dTedt
```

```
    ]

# initial condition
x0 = [sigma0x,sigma0z,1,1,0,Ti0,50]

# declare a time vector
time = np.linspace(0, 35, 1001)*1e-6
x = odeint(odes, x0, time)

sigmax = x[:,0]
sigmaz = x[:,1]
gammax = x[:,2]
gammaz = x[:,3]
Uii    = x[:,4]
Ti     = x[:,5]
Te     = x[:,6]


fig, ax = plt.subplots(1,1)
ax.plot(time/tauexp,Ti,label='asymmetrical')

#%%
# constants
kb     = 1.38e-23
mi     = 88*1.661e-27 # in kg
me     = 9.11e-31 # in kg
e      = 1.6e-19
eps0   = 8.85e-12
n0     = 1.1e15 * 0.5 # Killian paper Fig. 5 (a) # Changing this to 0.1e15
    brought it closer.
```

```
104 sigma0 = 0.001035
105 Ti0    = 0.002
106 #tauexp = 15e-6   # Killian paper Fig. 5 (a)
107 tauexp = np.sqrt(mi*sigma0**2/kb/(50)) # ours
108
109 def odes(x, t):
110
111   # assign each ODE to a vector element
112   sigma  = x[0]
113   gamma  = x[1]
114   Uii    = x[2]
115   Ti     = x[3]
116   Te     = x[4]
117
118
119   # define other variables
120 #  n      = n0/(1+t**2/tauexp**2)**(3/2)#*np.exp(-1/2) # Includes 't'. #
    Having the extra term improved the accuracy.
121   n = n0 * (sigma0**2 / sigma**2)**(3/2)
122   aws    = (4*np.pi*n/3)**(-1/3)
123   omega  = np.sqrt(n*e**2/me/eps0)
124   tau    = np.sqrt(mi*eps0/e**2/n)
125   Gammae = e**2/(4*np.pi*eps0*aws)/(kb*Te)
126   Lambda = 1/np.sqrt(3)/Gammae**(3/2)
127   gammaei = np.sqrt(np.pi) * np.sqrt(2/(3*np.pi))*Gammae**(3/2)*omega*np.
    log(Lambda) ###################################
128 #  gammaei = 0
129   Gamma  = e**2/(4*np.pi*eps0*aws)/(kb*Ti)
130   A1     = -0.9052 # The numbers here do not make significant change
131   A2     = 0.6322  # The numbers here do not make significant change
```

```
132   A3      = -np.sqrt(3)/2-A1/np.sqrt(A2)
133   Uiieq   = kb*Ti*Gamma**(3/2)*(A1/np.sqrt(A2+Gamma)+A3/(1+Gamma))
134
135
136   # define each ODE
137   dsigmadt = gamma*sigma
138   dgammadt = (kb*Te+Uii/3)/(mi*sigma**2)-gamma**2
139   dUiidt = -(Uii-Uiieq)/tau
140 #  dUiidt = 0
141   # From Killian
142   dTidt = -2*gamma*Ti-2/3/kb*(gamma*Uii+dUiidt)+2*me/mi*gammaei*Te
143   # The equation we derived from PPR
144 #  dTidt = -2*gamma*Ti-2/3/kb*gamma*Uii+2/kb*dUiidt+2*me/mi*gammaei*Te
145   dTedt = -2*gamma*Te-2*me/mi*gammaei*Te
146
147
148   return [dsigmadt, dgammadt, dUiidt, dTidt, dTedt]
149
150 # initial condition
151 x0 = [sigma0,1,0,Ti0,50]
152
153
154 # declare a time vector
155 time = np.linspace(0, 35, 1001)*1e-6
156 x = odeint(odes, x0, time)
157
158 sigma   = x[:,0]
159 gamma   = x[:,1]
160 Uii     = x[:,2]
161 Ti      = x[:,3]
```

```
Te      = x[:,4]

# Below are with trouble shooting
ax.plot(time/tauexp,Ti,label='symmetrical')
ax.set_xlabel('time/$\\tau_{exp}$')
ax.set_ylabel('$T_i$ ' + '(K)')
plt.legend()
plt.tight_layout()
fig.show()
```

Listing A.1 Python code for solving the differential equations from the McQuillen et. al. paper [8].

Bibliography

[1] T. C. Killian, T. Pattard, T. Pohl, and J. Rost, "Ultracold neutral plasmas," Physics Reports **449,** 77–130 (2007).

[2] M. Lyon and S. Rolston, "Ultracold neutral plasmas," Reports on Progress in Physics **80,** 017001 (2016).

[3] S. D. Bergeson, S. D. Baalrud, C. L. Ellison, E. Grant, F. R. Graziani, T. C. Killian, M. S. Murillo, J. L. Roberts, and L. G. Stanton, "Exploring the crossover between high-energy-density plasma and ultracold neutral plasma physics," Physics of Plasmas **26,** 100501 (2019).

[4] T. Killian, S. Kulin, S. Bergeson, L. A. Orozco, C. Orzel, and S. Rolston, "Creation of an ultracold neutral plasma," Physical Review Letters **83,** 4776 (1999).

[5] T. Pohl, T. Pattard, and J. M. Rost, "Kinetic modeling and molecular dynamics simulation of ultracold neutral plasmas including ionic correlations," Physical Review A **70,** 033416 (2004).

[6] E. Cummings, J. Daily, D. S. Durfee, and S. D. Bergeson, "Ultracold neutral plasma expansion in two dimensions," Physics of plasmas **12,** 123501 (2005).

[7] T. Pohl, T. Pattard, and J. Rost, "Relaxation to nonequilibrium in expanding ultracold neutral plasmas," Physical review letters **94,** 205003 (2005).

[8] P. McQuillen, T. Strickler, T. Langin, and T. Killian, "Ion temperature evolution in an ultracold neutral plasma," Physics of Plasmas **22,** 033513 (2015).

[9] M. Lyon and S. Bergeson, "The influence of electron screening on disorder-induced heating," Journal of Physics B: Atomic, Molecular and Optical Physics **44,** 184014 (2011).

[10] P. Gupta, S. Laha, C. Simien, H. Gao, J. Castro, T. Killian, and T. Pohl, "Electron-temperature evolution in expanding ultracold neutral plasmas," Physical review letters **99,** 075005 (2007).

[11] S. D. Bergeson, A. Denning, M. Lyon, and F. Robicheaux, "Density and temperature scaling of disorder-induced heating in ultracold plasmas," Physical Review A **83,** 023409 (2011).

[12] J. Castro, P. McQuillen, and T. Killian, "Ion acoustic waves in ultracold neutral plasmas," Physical Review Letters **105,** 065004 (2010).

[13] T. Killian, P. McQuillen, T. O'Neil, and J. Castro, "Creating and studying ion acoustic waves in ultracold neutral plasmas," Physics of Plasmas **19,** 055701 (2012).

[14] X. Zhang, R. Fletcher, S. Rolston, P. Guzdar, and M. Swisdak, "Ultracold plasma expansion in a magnetic field," Physical review letters **100,** 235002 (2008).

[15] G. M. Gorman, M. Warrens, S. Bradshaw, and T. Killian, "Magnetic confinement of an ultracold neutral plasma," Physical Review Letters **126,** 085002 (2021).

[16] R. T. Sprenkle, S. Bergeson, L. G. Silvestri, and M. S. Murillo, "Ultracold neutral plasma expansion in a strong uniform magnetic field," Physical Review E **105,** 045201 (2022).

[17] T. Ott, H. Löwen, and M. Bonitz, "Dynamics of two-dimensional one-component and binary Yukawa systems in a magnetic field," Physical Review E **89,** 013105 (2014).

[18] T. Ott and M. Bonitz, "Diffusion in a strongly coupled magnetized plasma," Physical review letters **107,** 135003 (2011).

[19] T. Ott, H. Kählert, A. Reynolds, and M. Bonitz, "Oscillation spectrum of a magnetized strongly coupled one-component plasma," Physical Review Letters **108,** 255002 (2012).

[20] M. R. Gomez *et al.*, "Experimental demonstration of fusion-relevant conditions in magnetized liner inertial fusion," Physical review letters **113,** 155003 (2014).

[21] S. D. Baalrud and J. Daligault, "Transport regimes spanning magnetization-coupling phase space," Physical Review E **96,** 043202 (2017).

[22] F. Boeschoten, "Review of experiments on the diffusion of plasma across a magnetic field," Journal of Nuclear Energy. Part C, Plasma Physics, Accelerators, Thermonuclear Research **6,** 339 (1964).

[23] F. Hoh, "Low-temperature plasma diffusion in a magnetic field," Reviews of Modern Physics **34,** 267 (1962).

[24] S. Harilal, M. Tillack, B. O'shay, C. Bindhu, and F. Najmabadi, "Confinement and dynamics of laser-produced plasma expanding across a transverse magnetic field," Physical Review E **69,** 026413 (2004).

[25] G. Serianni *et al.*, "Coherent structures and transport properties in magnetized plasmas," Plasma Physics and Controlled Fusion **49,** B267 (2007).

[26] J. M. Guthrie and J. L. Roberts, "Finite-amplitude RF heating rates for magnetized electrons in neutral plasma," Physics of Plasmas **28,** 052101 (2021).

[27] T. Ott, M. Bonitz, and Z. Donko, "Effect of correlations on heat transport in a magnetized strongly coupled plasma," Physical Review E **92,** 063105 (2015).

[28] S. Lebedev *et al.*, "The formation of reverse shocks in magnetized high energy density supersonic plasma flows," Physics of Plasmas **21,** 056305 (2014).

[29] K. Matsuo *et al.*, "Magnetohydrodynamics of laser-produced high-energy-density plasma in a strong external magnetic field," Physical Review E **95,** 053204 (2017).

[30] S. K. Tiwari and S. D. Baalrud, "Reduction of electron heating by magnetizing ultracold neutral plasma," Physics of Plasmas **25,** 013511 (2018).

[31] B. Scheiner and S. D. Baalrud, "Viscosity of the magnetized strongly coupled one-component plasma," Physical Review E **102,** 063202 (2020).

[32] T. Lafleur and S. D. Baalrud, "Friction in a strongly magnetized neutral plasma," Plasma Physics and Controlled Fusion **62,** 095003 (2020).

[33] S. D. Baalrud and J. Daligault, "Temperature anisotropy relaxation of the one-component plasma," Contributions to Plasma Physics **57,** 238–251 (2017).

[34] C. Lisdat, J. V. Winfred, T. Middelmann, F. Riehle, and U. Sterr, "Collisional losses, decoherence, and frequency shifts in optical lattice clocks with bosons," Physical Review Letters **103,** 090801 (2009).

[35] T. Kisters, K. Zeiske, F. Riehle, and J. Helmcke, "High-resolution spectroscopy with laser-cooled and trapped calcium atoms," Applied Physics B **59,** 89–98 (1994).

[36] F. Ruschewitz, J. Peng, H. Hinderthür, N. Schaffrath, K. Sengstock, and W. Ertmer, "Sub-kilohertz optical spectroscopy with a time domain atom interferometer," Physical review letters **80,** 3173 (1998).

[37] C. W. Oates, F. Bondu, R. W. Fox, and L. Hollberg, "A diode-laser optical frequency standard based on laser-cooled Ca atoms: Sub-kilohertz spectroscopy by optical shelving detection," The European Physical Journal D-Atomic, Molecular, Optical and Plasma Physics **7,** 449–460 (1999).

[38] M. H. Anderson, J. R. Ensher, M. R. Matthews, C. E. Wieman, and E. A. Cornell, "Observation of Bose-Einstein condensation in a dilute atomic vapor," science **269,** 198–201 (1995).

[39] K. B. Davis, M.-O. Mewes, M. R. Andrews, N. J. van Druten, D. S. Durfee, D. Kurn, and W. Ketterle, "Bose-Einstein condensation in a gas of sodium atoms," Physical review letters **75,** 3969 (1995).

[40] A. J. Daley, M. M. Boyd, J. Ye, and P. Zoller, "Quantum computing with alkaline-earth-metal atoms," Physical review letters **101,** 170504 (2008).

[41] M. Foss-Feig, M. Hermele, and A. M. Rey, "Probing the Kondo lattice model with alkaline-earth-metal atoms," Physical Review A **81,** 051603 (2010).

[42] A. V. Gorshkov, M. Hermele, V. Gurarie, C. Xu, P. S. Julienne, J. Ye, P. Zoller, E. Demler, M. D. Lukin, and A. Rey, "Two-orbital SU (N) magnetism with ultracold alkaline-earth atoms," Nature physics **6,** 289–295 (2010).

[43] P. Halder, H. Winter, and A. Hemmerich, "Inelastic collisions of optically trapped metastable calcium atoms," Physical Review A **88,** 063639 (2013).

[44] D. P. Hansen, J. R. Mohr, and A. Hemmerich, "Magnetic trapping of metastable calcium atoms," Physical Review A **67,** 021401 (2003).

[45] J. Grünert and A. Hemmerich, "Sub-Doppler magneto-optical trap for calcium," Physical Review A **65,** 041401 (2002).

[46] H. J. Metcalf and P. Van der Straten, *Laser cooling and trapping* (Springer Science & Business Media, 1999).

[47] R. Senaratne, S. V. Rajagopal, Z. A. Geiger, K. M. Fujiwara, V. Lebedev, and D. M. Weld, "Effusive atomic oven nozzle design using an aligned microcapillary array," Review of Scientific Instruments **86,** 023105 (2015).

[48] Y. Yu and A. Derevianko, "Transition rates and radiative lifetimes of Ca I," Atomic Data and Nuclear Data Tables **119,** 263–286 (2018).

[49] M. Mills, P. Puri, Y. Yu, A. Derevianko, C. Schneider, and E. R. Hudson, "Efficient repumping of a Ca magneto-optical trap," Physical Review A **96,** 033402 (2017).

[50] M. Lyon and S. Bergeson, "Precision spectroscopy using a partially stabilized frequency comb," Applied Optics **53,** 5163–5168 (2014).

[51] C. Pak, M. J. Schlitters, and S. D. Bergeson, "Improved ionization potential of calcium using frequency-comb-based Rydberg spectroscopy," Physical Review A **106,** 062818 (2022).

[52] J. Ye, S. Swartz, P. Jungner, and J. L. Hall, "Hyperfine structure and absolute frequency of the 87 Rb 5P 3/2 state," Optics letters **21,** 1280–1282 (1996).

[53] J. Jin and D. Church, "Precision lifetimes for the Ca+ 4p 2 P levels: Experiment challenges theory at the 1% level," Physical review letters **70,** 3213 (1993).

Index